

Vision-Based Autonomous Ground Vehicle Navigation

Michael Koval

mkoval@eden.rutgers.edu

Electrical and Computer Engineering

May 2, 2011

1 Introduction

The Intelligent Ground Vehicle Competition (IGVC) is an international collegiate robotics competition that tasks each team to design, build, and program a fully autonomous mobile ground vehicle. Each successful entry must autonomously navigate through an outdoor obstacle course using only the sensors and computing power on-board the robot. As per the official rules, the competition is split into three parts: (1) navigating through a narrow obstacle course delimited by painted white lines, (2) traveling between global positioning system (GPS) waypoints scattered throughout a large field, and (3) responding to Joint Architecture for Unmanned Systems (JAUS) messages to autonomous control the robot [12].

For each of these tasks, the robot is provided with only the GPS coordinates of a destination way point and has knowledge of the course's topology. Without a priori knowledge of the course boundaries and obstacles, navigating to the destination requires that the robot build a map of its environment in real-time. Using this map, the robot can plan a path through the drivable regions of the course towards the final destination, avoiding obstacles and avoiding the course boundaries at all costs. While the accuracy requirements for the perception and localization algorithms used to build a global map are significantly higher than simpler techniques, navigating with no high-level view of the environment is much less effective.

Adding obstacles to the robot's internal representation of the world is accomplished by merg-

ing the output of a scanning laser range finder (LIDAR) and a custom stereo camera. In addition to identifying road obstacles, a successful entry must also employ monocular image processing techniques to identify the painted white lines that mark the course boundaries. Before discussing specific obstacle and line detection algorithms, Section 2 provides a brief introduction to the hardware and software powering the Rutgers Navigator, Rutgers University's entry into the 2011 IGVC. The remainder of this paper is split into two major sections: stereo reconstruction (Section 3) for obstacle detection and monocular image processing (Section 4) for detecting the course boundary lines (Section Finally, Section 6 discusses the global impact of robotics: how robots can assist in the recovery from major environmental disasters, such as the recent earthquake off the coast of Japan.

2 Rutgers Navigator

Designed specifically for rugged outdoor use and modularity, the Rutgers Navigator (Figure 1) is constructed entirely out of 80/20 extrusion and custom-machined aluminum stock. This provides a strong, light¹ frame that is much easier to modify than a conventional welded steel frame. This chassis is supported by three wheels: two powered front wheels that are mounted on a wish bone suspension for improved stability and free-spinning rear caster chosen specifically to reduce friction while turning.

¹Approximately 100 lb empty and 150 lb fully loaded.



Figure 1: Rutgers Navigator. The front of the robot is equipped with three stereo stereo cameras on the front of the robot, and one camera located above each front wheel (not visible).

2.1 Sensing Capabilities

Each of the four drive motors attached to the powered front wheels is equipped with an internal hall-effect quadrature encoder to measure wheel speed and a current sensor to monitor power consumption. The local odometry information captured by the wheel encoders is combined with the data produced by a nine-axis inertial measurement unit (IMU) to estimate the robot’s motion. Between the wheel encoders, accelerometer, gyroscope, and magnetometer, the Navigator has access to a wealth of inertial data about its motion. Unfortunately, all of these sensors share a common flaw: the tendency to drift over time by accumulating correlated error. Without frequent zeroing the Navigator’s position estimate to a known location, this type of localization quickly becomes too inaccurate for long-term mapping.

To correct for the encoder and IMU drift, the Navigator uses a differential global positioning system (DGPS) to measure its position in a globally fixed coordinate frame. Using publicly available differential correction signals provided by the United States Coast Guard, the high-end Novatel DGPS on the Navigator is capable of estimating the robot’s position anywhere on the Earth within 50 cm. Combined with OmniStar’s professional DGPS correction service, the Novatel DGPS’s accuracy increases to approximately 10 cm: a localization error that is insignificant

compared to the size of the robot. By fusing the DGPS and the inertial position estimates with an enhanced Kalman filter, the Navigator will both have an accurate estimate of its absolute position and its relative motion over time.

As was discussed in Section 1, precise knowledge of the robot’s position is not sufficient to perform well in any of the IGVC challenges. To detect obstacles in its environment, the Navigator uses the combination of a high-end Hokuyo scanning laser rangefinder (LIDAR) and a custom trinocular stereo camera that is discussed in detail in Section 3. Combining the high-resolution planar data returned by the Hokuyo LIDAR with the stereo reconstruction of the scene, the navigator can take advantage of the best features of both technologies: the Hokuyo’s 270 degree horizontal field of view and the stereo cameras’ 75 degree vertical field of view. In addition to the Hokuyo LIDAR and trinocular stereo camera, an additional angled camera is mounted above each front wheel to identify painted boundary lines that cannot be seen by the stereo cameras.

2.2 Software Architecture

Interaction between the robot’s individual software components is managed using the Robot Operating System (ROS), a framework developed by Willow Garage to promote code reuse in robotics. Besides providing a common interface to libraries such as OpenCV and PointCloud Library (PCL), ROS encourages the separation of software into a graph of loosely-coupled *nodes* that communicate over TCP/IP sockets. Because each node *subscribes* to its inputs and *publishes* its outputs with no global knowledge of the system, it is possible to reuse nodes without ever modifying their internal structure.

Figure 2 shows an overview of the flow of data between nodes in the computer vision subsystem. Within this graph of nodes, there are two distinct pipelines: stereo vision and monocular lane tracking. As its name suggests, the *stereo vision* pipeline (Section 3) uses triplets of synchronized images from the front stereo camera to generate a three-dimensional point cloud

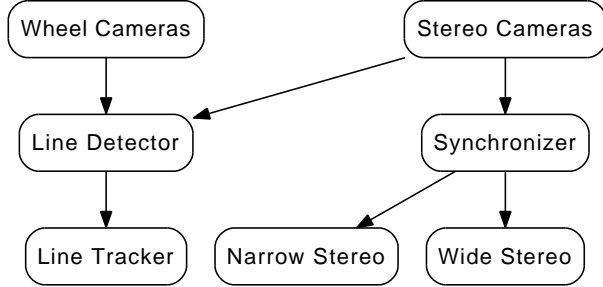


Figure 2: Computer vision software subsystem. Processing is split between the line detection pathway (left) and the stereo vision pathway (right).

of obstacles. The monocular *line tracking* (Section 4) pipeline, conversely, processes images from the left stereo camera and the two wheel cameras to find any white painted lines that are in the Navigator’s field of view. Detected lines are projected into three-dimensional space and are directly added to the global navigation grid as boundary obstacles.

3 Stereo Vision

Unlike a laser rangerfinder, such as the Hokuyo UTM-30LN that was discussed in Section 2, stereo vision is a passive sensor that reconstructs a three-dimensional scene using two or more standard cameras placed at different locations in space. By matching corresponding points between images captured by the two cameras and using knowledge of their relative positions in space (i.e. the *baseline*), it is possible to completely reconstruct a three-dimensional scene. While fairly straightforward with stationary cameras in a static scene, using stereo vision on a moving platform poses many more problems.

Before discussing the actual scene reconstruction, Section 3.1 discusses the process of *hardware synchronization* the Navigator’s trinocular stereo camera. This guarantees that the baseline remains constant even when the robot is driving at high speeds and allows stereo vision to reliably work on a moving platform. Assuming that the cameras are rigidly mounted and synchronized,

Section 3.2 discusses the selection of a trinocular stereo system with a 10 cm *narrow* baseline and 20 cm *wide* baseline the *baseline multiplexing* that fuses the data into a single reconstructed point cloud. Using the combined point cloud, Section 3.3 describes the base stereo reconstruction algorithm used for triangulation and Section 3.3.2 details the post-processing processing steps needed to identify obstacles in the reconstructed point cloud.

3.1 Synchronization

Stereo vision on a mobile robot is a non-trivial problem that has traditionally expensive, hardware-synchronized machine-vision cameras. Because standard stereo reconstruction assumes that the images from the left and right cameras are captured from a common scene, any motion that occurs between the left and right cameras capturing frames is equivalent to a change in the stereo camera’s baseline. This change in baseline invalidates the system’s extrinsic calibration², causing the quality of the rectification to decrease and the distances to be distorted by the robot’s velocity [5].

Hardware synchronization, the process of forcing two or more cameras to share a common hardware clock, has been traditionally limited to professional stereo vision systems such as Point Grey’s Bumblebee product line. Thankfully, the inexpensive Playstation Eye camera is built on the same high-end OmniVision OV7720 chipset that is comparable to those found in many machine vision cameras. These cameras can be hardware-synchronized using the exposed frame clock input (**FSIN**) and output (**VSYNC**) pins [1]. By shorting one camera’s **VSYNC** pin to the other cameras’ **FSIN** pins, the cameras are forced to share a common clock. To reduce the risk of a difference in ground potentials damaging the OV7720’s delicate circuitry, each camera was also modified to share a common ground.

This hardware synchronization guarantees that all three cameras capture images simultaneously, but does not guarantee that the

²Capturing images at 30 Hz while moving at 10 mph could change the baseline by up to 7 cm.

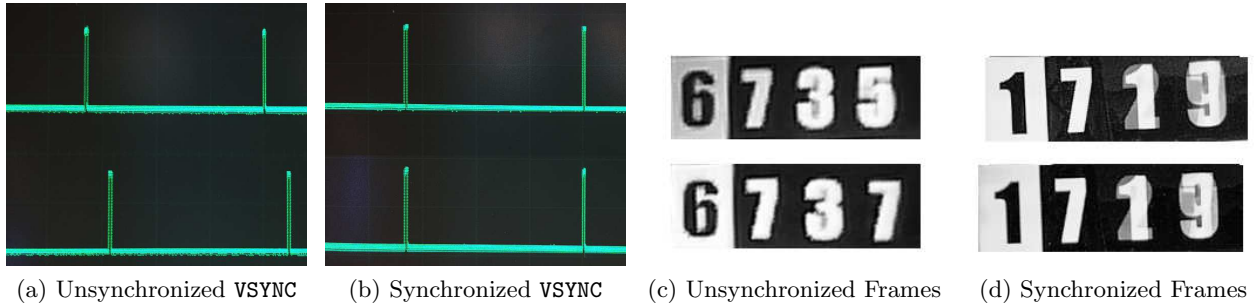


Figure 3: Verification of hardware and software camera synchronization for two Playstation Eye cameras. Note how only the synchronized cameras share a common VSYNC clock and capture identical readings of a millisecond resolution timer.

frames will remain synchronized after USB transfer to the computer. Making direct use of the Video4Linux kernel module, reliable synchronization was achieved by enabling memory-mapped I/O for image transferring and fuzzy-matching the Linux kernel’s USB transfer timestamps³. Because this matching algorithm uses the Linux kernel’s USB transfer timestamps instead of those measured in user-space, this simple algorithm is extremely robust to periodic desynchronizations caused by dropped frames and increased USB latency.

Hardware synchronization was verified by probing each camera’s VSYNC pin with an oscilloscope (Figures 3a and 3b) and confirming that all three clocks are in phase. The software synchronization was further verified by simultaneously capturing images of a millisecond resolution timer (Figures 3c and 3d on all three synchronized cameras). Since the times exactly match after synchronization and differ by several milliseconds on the original unsynchronized cameras, the camera synchronization is clearly a success. These three hardware-synchronized Playstation Eye cameras are mounted in a custom polycarbonate case on the front of the Navigator and serve as a custom trinocular stereo camera.

3.2 Baseline Selection

Selecting the optimal baseline for a stereo system is a balance of two opposing, but equally important, factors: field of view and maximum range. Decreasing the baseline increases the shared field of view of the two cameras at the cost of a shorter maximum range. Conversely, increasing the baseline decreases the aggregate field of view, but yields an increased maximum range and better precision at each visible distance. Using a trinocular stereo system instead of a standard binocular system allows the software to get the advantages of two baselines with the addition of only one camera.

The *narrow* pair has a baseline of approximately 10 cm and uses the left and middle cameras. Conversely, the *wide* pair has a baseline of approximately 20 cm and uses the left and right cameras. By using the narrow baselines for nearby points and the wide baseline for more distance points, this trinocular stereo system combines the small minimum range of the narrow baseline with the better accuracy and maximum range of the wide baseline.

3.3 Reconstruction Algorithm

Due to the use of ROS as the basis for the Navigator’s software architecture (Section 2), the actual stereo reconstruction is done using the standard `stereo_image_proc` ROS node. Before being processed for point correspondences, the pair of input images is rectified, regions of low

³https://github.com/mkoval/stereo_webcam



(a) Multiplexed Point Cloud

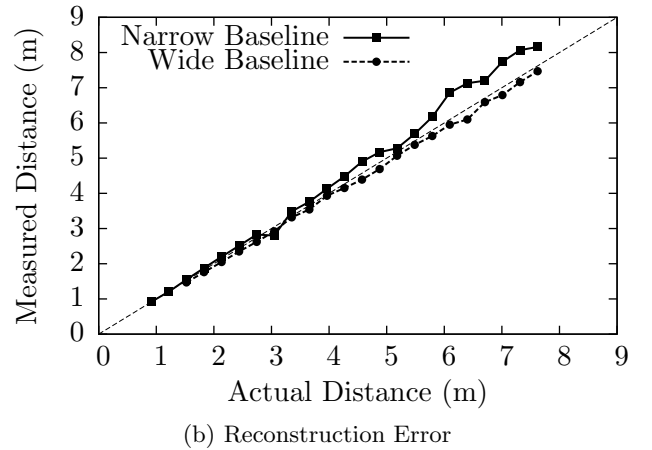


Figure 4: Reconstructed point cloud using stereo multiplexing. Differences in the camera’s rectification and reconstruction accuracy cause a small rotation in the reconstructed point cloud.

texture are masked out, and a Sobel filter is applied to amplify texture [8]. Each pixel in the left image is matched to the most similar pixel in the corresponding row in the right image using a sum-of-squared difference (SSD) block-matching algorithm [8] and the corresponding disparity is calculated. This disparity is then converted to a three-dimensional point using the camera’s intrinsic parameters.

While more efficient than the graph-cut based alternatives, [8] the SSD block-matching algorithm implemented in the ROS `stereo_image_proc` is still extremely computationally intensive. With all three cameras set to a resolution of 640×480 and a frame rate of 15 Hz, the stereo block-matching algorithm runs at approximately 10-12 Hz. While this is much slower than the 60 Hz maximum frame rate of the cameras, it is more than sufficient considering the rate at which the path planning algorithm executes.

3.3.1 Ground Plane Detection

When travelling over uneven terrain such as grass, the position and orientation of the cameras can change relative to the ground as the robot moves. Compounded by perspective projection, the effect of this movement is very detrimental to algorithms that rely on knowledge of the

ground plane such as stereo obstacle detection (Section 3.3.2) and the matched pulse-width filter used for line detection (Section 4). Analysis of recorded video that has been processed by the above reconstruction algorithm shows that the block-matching algorithm described in Section 3.3 detects sufficient texture on the ground to produce a dense disparity map.

Assuming that the ground is a perfect plane parameterized by a, b, c , and d , a large number of reconstructed points are described by the model

$$ax + by + cz + d = 0, \quad (1)$$

where (x, y, z) are the reconstruction points position in three-dimensional space.

Once stereo vision has reconstructed the three-dimensional scene in front of the Navigator, the Random Sample and Consensus (RANSAC) model-fitting algorithm is used to fit Equation 1 to the ground plane. Unlike least-squares estimation and other primitive model-fitting algorithms, RANSAC is a robust iterative algorithm that *randomly samples* the data to find a model that minimizes the model error for some *consensus set* of inliers. Assuming that the ground plane is the dominant plane in the image and that RANSAC is run for a sufficient number of iterations, RANSAC classifies points on the ground plane as inliers and all other points, such as obstacles, as outliers.

Unfortunately, the assumption that the ground plane will dominate other planes in the image is only accurate if the region in front of the robot is relatively empty. When the robot is facing a nearby obstacle, RANSAC may inappropriately fit a plane to obstacle points instead of the non-existent ground points. Since such a situation would rotate the ground plane by approximately 90 degrees, a manually-tuned decision tree is used to reject poor fits. This decision tree eliminates models that have too few inliers, are at too high of an angle, or have too large a vertical offset from the robot. Simulation and experimental testing using a heavily textured plane show that this decision tree eliminates the vast majority of false ground plane detections.

3.3.2 Obstacle Detection

Once the ground plane has been found and the inlier points have been removed, the remainder of the point cloud is assumed to be a mix of obstacle points and outliers caused by incorrect point correspondances. As the Navigator uses a path planner that does not explicitly deal with uncertainty, these false positives must be removed before detected obstacles are added to the map used for path planning.

Assuming that correctly detected obstacles dominate the remaining points, the obstacle detection problem is reduced to an outlier detection on a three-dimensional point cloud. Properly reconstructed points that belong to an object are likely to form large clusters and outliers are likely to remain fairly isolated. If an obstacle point is selected at random, one would expect that the standard deviation of the x , y , and z coordinates of its k nearest neighbors to be relatively low. For an isolated outlier, the same calculation would produce an abnormally high standard deviation [10]. By repeating this process on every point and classifying all points with a sufficiently high standard deviation as outliers, spurious detections from poor point correspondances are completely eliminated [10]. Once outliers have been removed, the resultant point cloud can safely be added to the robot's internal map.

3.4 Error Analysis

After the stereo cameras were calibrated using a modified version of the ROS camera calibration toolkit, the depths reported by both stereo baselines were measured and compared to ground truth. Measuring the ground truth data from 0 to 8 meters (Figure 4), the narrow stereo pair's dead zone of 0.9 meters is approximately half the size of the wide stereo pair's dead zone of 1.6 m. As distance increases beyond 3 m, the wide baseline begins to surpass the narrow baseline in accuracy. In addition to manual measurements with a calibration chessboard, these results were confirmed by using the Hokuyo LIDAR for ground-truth distances. Even when objects are several meters away, the depths calculated by the stereo vision system match those measured by the Hokuyo LIDAR within several inches.

4 Lane Tracking

For both the navigation and GPS challenges, the drivable region of the course is delimited by a three inch wide line painted on grass or asphalt. Robustly identifying and tracking these boundary lines is a difficult problem that has been the primary cause of disqualification in previous years of competitions. For example, 28 out of 29 competitors were disqualified failing to move, leaving the course, or striking an obstacle before five minutes time limit elapsed in the 2010 IGVC.

To avoid repeating the errors made by teams in previous years, the Navigator simultaneously runs an advanced line detection algorithm on images from three cameras: the center stereo camera, the left wheel camera, and the right wheel camera. The front-facing stereo camera provides the long-term knowledge of the course shape necessary for path planning, while the left and right insure that the Navigator does not inadvertently cross a line while following a long-term path. By fusing the line detection results from all three cameras, the Navigator's field of view is expanded from 75 degrees to nearly a full 180 degrees.

The line detection algorithm run in parallel on each camera is a modified version of the algorithm used by Massachusetts Institute of Technology's entry into the DARPA Grand Challenge. In this algorithm, a color image of the course first undergoes a color space transformation to emphasize white regions of the image (Section 4.2). The grayscale output of the color space transformation is then filtered using a matched pulse-width filter (Section 4.3) that eliminates lines of the incorrect width. Finally, the size of the output point cloud is compressed using non-maximal suppression (Section 4.4) and the detected local maxima are transformed into the world coordinate frame to be directly used for navigation [6] [7].

4.1 Extrinsic Calibration

While the addition of two wheel cameras greatly expands the Navigator's field of view, the images are only useful if they are captured in a known coordinate frame. As the stereo camera is calibrated against the LIDAR, the extrinsic calibration of the wheel cameras can be simplified to finding their pose relative to the stereo camera. Using a process common in calibration, a small chessboard is placed in the shared field of view of the two cameras. Each of the detected grid corners, p_1, p_2, \dots, p_n are assigned three-dimensional coordinates in a coordinate frame aligned with the chessboard: P_1, P_2, \dots, P_n .

Using the camera's intrinsic matrix and the definition of perspective projection, the relationship

$$\tilde{p}_i = M_{int} T \tilde{P}_i$$

must hold for each point, where T is the transformation from the chessboard frame to the camera frame. Expanding the matrix multiplication $T\tilde{P}_i$, this can be rewritten as $M_{int}^{-1}\tilde{p}_i = T\tilde{P}_i$ and T is found using least-squares estimation.

To calibrate one camera relative to second camera, this calibration procedure is repeated on a pair of synchronized frames. Since the same chessboard is seen in both views, T_1 is the transformation from the chessboard to camera 1 and T_2 is the transformation from the same chessboard to camera 2. Both transformations are

expressed in a common coordinate frame and the transformation from camera 2 to camera 1 is simply $T_{12} = T_1 T_2^{-1}$. Using this calibration technique to solve for the position of the left and right wheel cameras relative to the center stereo camera makes it possible to accurately transform coordinates generated in all three cameras into a common coordinate frame that can be used for navigation.

4.2 Color Space Transformation

Using a priori knowledge that the lines are white, the first step towards effectively isolating them from their surroundings is to convert the rectified color image into a monochromatic color space where white is amplified. Because white is inherently of high intensity and low saturation, the hue-saturation-value (HSV) color space is a natural choice. If the original image, I_{orig} , has the 8-bit HSV channels $H(x, y)$, $S(x, y)$, and $V(x, y)$, define the pre-processed image I_{pre} to be

$$I_{pre}(x, y) = \min \{255 - S(x, y), V(x, y)\}$$

for each pixel (x, y) in I_{orig} .

4.3 Matched Pulse-Width Filter

In addition to the lines' color, the 2011 IGVC rules specify that all painted lines will be uniformly three inches wide. Using this knowledge of the line's width, an obvious approach for isolating them from other objects is to use a digital *pulse-width filter* that responds strongly to objects with the same width as a line. Unfortunately, effect of perspective projection causes the apparent width of lines in an image depend upon their distance from the camera and position in three-dimensional space. To obtain meaningful output, such a filter must be properly *matched* to expected width of the line for each point in the input image [6] [7].

Calculating this width requires knowledge of the three-dimensional point corresponding to each pixel in the image. Assuming that the ground plane is known and is parametrized by point P and normal n , the three-dimensional

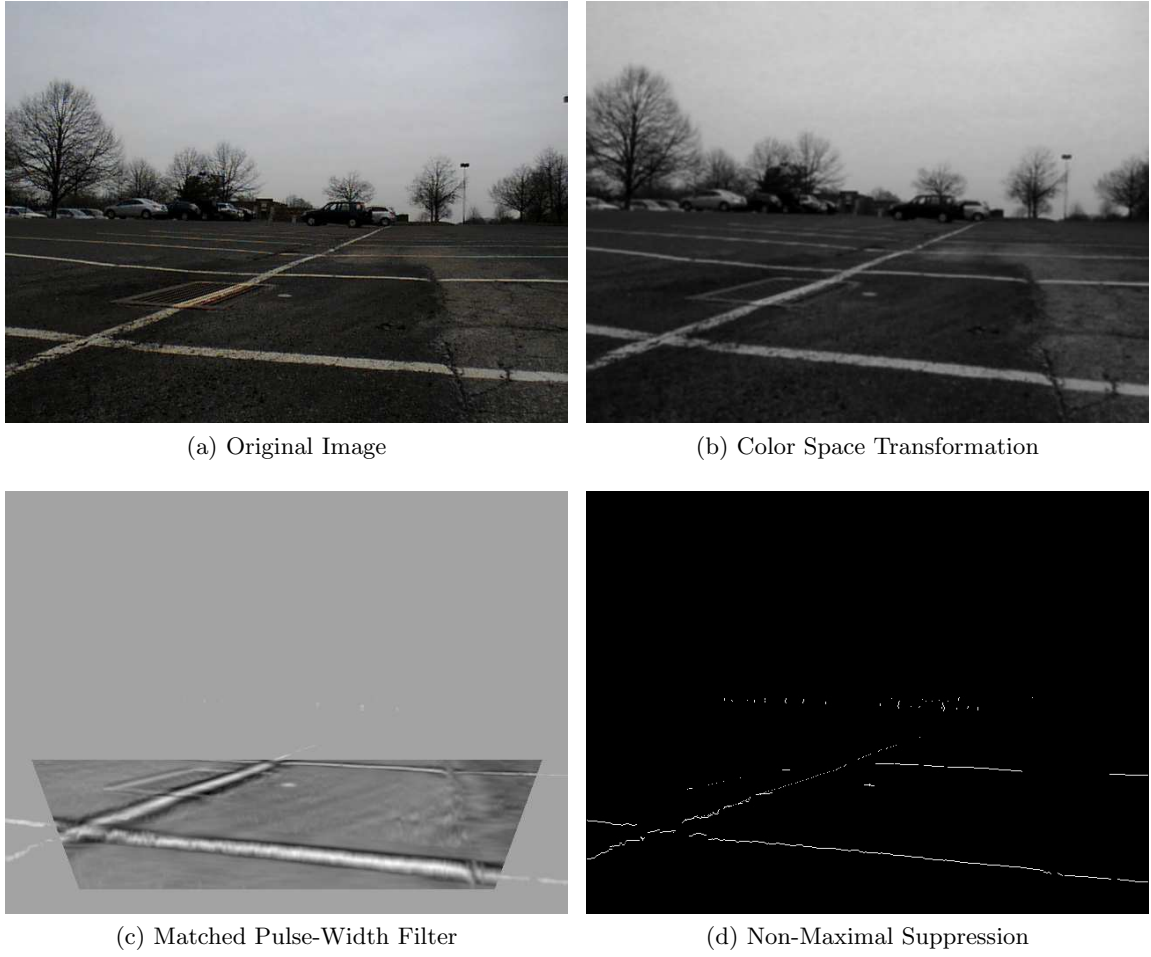


Figure 5: Intermediate stages of the line detection algorithm. Each stage of processing removes filters unnecessary data from the image and simplifies the remainder of the processing pipeline.

point P that corresponds to pixel p satisfies both

$$(P - P_0) \cdot n = 0$$

$$\lambda M_{int}^{-1}p - \tilde{P} = 0,$$

where M_{int} is the camera's intrinsic matrix and λ is an arbitrary constant.

Solving for λ gives a closed-form expression expressed in terms of only known parameters. Substituting this definition of λ into the equation of the line yields an intersection point of

$$P = \left(\frac{n \cdot \tilde{P}_0}{n \cdot M_{int}^{-1}p} \right) M_{int}^{-1}p.$$

Using the new-found knowledge of point P , the length of an arbitrary real-world vector projected

into the image at point p is

$$\delta = \|M_{int}\tilde{P} - M_{int}(\tilde{P} + \Delta)\|_2 \quad (2)$$

where δ is the image distance corresponding to a change in world coordinates by the vector Δ and $\|\cdot\|_2$ denotes the Euclidean norm. Note that this is not equivalent to $\|M_{int}\Delta\|_2$ because of the division implicit in the use of homogeneous coordinates.

Using this equation, the four distances of interest depicted in Figure 6 are projected into the image using Equation 2. Of these four distances, δ_{LL} and δ_{LR} correspond to the left and right edges of the line, respectively. Similarly, δ_{BL} and δ_{BR} correspond to the expected total width of the filter (including a dead zone around

the line). Note that the filter is only symmetric (i.e. $\delta_{LL} = \delta_{LR}$ and $\delta_{BL} = \delta_{BR}$) for the horizontal filter kernel. The vertical filter is asymmetric and shifted due to perspective projection disproportionately elongating distances that are closer to the camera.

Once the four widths have been projected into the image, a filter kernel is constructed such that each of the negative *supports* sums to -0.5 and the central *pulse* sums to $+1.0$. This causes the filter to have a zero response on solid color and to only respond strongly to lines of the correct width and orientation. The region surrounding each pixel in the image is convolved with both the horizontal and vertical matched filters and the responses are ready for post-processing.

4.4 Non-Maximal Suppression

The matched pulse-width filter is extremely effective at isolating the line in the image, but does not produce a clean enough output to be directly used for model-fitting. In particular, the nature of digital filters guarantees that there will be weak, spurious responses near true positives.

Inspired by Canny edge detection, non-maximal suppression is an effective and computationally efficient way of reducing such a response to a single point. Considering the rows of the horizontally filtered image and the columns of the vertically filtered image, a pixel is considered a maximum if and only if it has a higher filter response than both of its neighbors. The maxima are then thresholded to discard those that do not exhibit a sufficiently strong filter response. This threshold was tuned to favor false positives and was set to approximately 15% of the filter's maximum response.

4.5 Error Analysis

Largely because this algorithm is rooted in physical constants, and has few arbitrary thresholds, this line detection algorithm works equally well in simulation and on real data.

Constructing the matched pulse-width filters succeeds even with large variations in the ground plane, but those filters no longer match the width

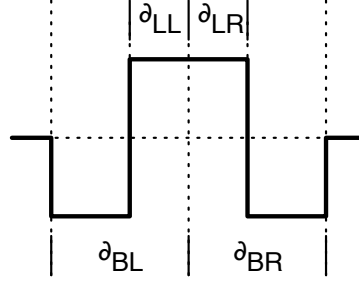


Figure 6: Sketch of the matched pulse-width filter's kernel. Note that $\delta_{LL} = \delta_{LR}$ and $\delta_{BL} = \delta_{BR}$ only for the horizontal kernel.

of the line in the image. Even worse, the detected line points in the world appear at the wrong distance from the image. Tested on both simulated data and real data, the algorithm appears very effective at identifying lines even in noisy environments (e.g. the parking lot in Figure 5).

5 Conclusion

After extensive testing of the custom stereo camera using an oscilloscope, a millisecond resolution timer, and outdoor data, it is clear that the three cameras are well synchronized. This synchronization translates into an extremely high quality reconstruction while the robot is moving, giving it the rich three-dimensional information required for path planning. Applying a matched pulse-width filter to detect the lines bordering the field successfully corrects for the effects of perspective transform and reliably detects both horizontal and vertical lines in the image.

6 Current Trends in Robotics

The recent Japanese earthquake and tsunami was one of the worlds' most devastating natural disasters. While the Japanese people's efficient response captivated international news, it rapidly became clear manual search and rescue is not feasible on a large scale. Every volunteer slowly climbs through debris of collapsed buildings, moving a few miles per hour and putting his or her own life at risk. This means that rescue volunteers are restricted to areas that have

been deemed sufficiently safe to walk: potentially denying access to some of the survivors who are in most urgent need of assistance.

One solution to the search and rescue problem is to deploy teleoperated tank-like robots to search debris for survivors [2]. While still controlled by a human, these search and rescue robots are equipped with infrared cameras and carbon dioxide sensors to detect the presence of humans that would otherwise go unnoticed [2]. Even better, this type of robot completely eliminates the need for rescue workers to enter dangerous areas: it can be remotely deployed and controlled from a safe distance without putting any emergency workers to risk. While these robots are not revolutionary, they do have a past history of success for mine rescues [9] and on September 11th [11].

While these robots remove human rescue workers from harms way, each robot is too costly to be deployed in bulk. Replacing one large robot with a large number of inexpensive, “disposable”, robots is a better solution for exploring dangerous environments such as collapsed buildings. One research group at the University of California at Berkeley has developed just that: an extremely inexpensive “mechanical cockroach” that is capable of fitting through small cracks in rubble [4]. Based on the principles of swarm robotics, using a large number of simple robots can give a cheaper and more robust system than a small number of expensive robots. This is especially the case in search and rescue: covering a wide area and being robust to extreme environmental conditions is much more important than access to expensive, high-accuracy sensing equipment. Even if a number of the robots are destroyed, the remaining robots are completely independent and can continue to aid the rescue effort.

For either of these techniques to become practical, the next major efficiency improvement will be from replacing the human teleoperator with a fully autonomous control system. This is especially important when using swarm robotic rescue system: while it may be feasible to have a dedicated teleoperator for a few smaller robots, it is completely infeasible for a large-scale swarm

system. Once the necessary advances have been made in producing inexpensive mobile robots, a completely autonomous swarm robotics rescue system will be the ideal solution for search and rescue: it is inexpensive, requires little supervision, and allows humans to focus on tasks that are not as easy to automate.

Search and rescue is only the first step in disaster recovery. Once the immediate disaster response is complete, the affected governments must begin the long and arduous process of repairing and replacing their damaged infrastructure. With the extent of damage caused by a natural disaster on the scale of the Japanese earthquake, it is not safe to open roads, bridges, or tunnels until they have been fully inspected and deemed structurally stable. This, unfortunately, means that engineers must enter the compromised (and potentially dangerous) structure to search for damage. Just like search and rescue, this is a natural task for a teleoperated robot.

Instead of the engineers directly inspecting the damage, a robot can be remotely controlled from a safe distance away from the damaged structure. Even better, the inspection robot can carry sensors that a human cannot. These might include a high-resolution camera [3] for inspecting damage to beams, a scanning laser rangefinder for building a three-dimensional model of the damage, or even a sensor package for measuring the concentration of airborne contaminants. This type of remote inspection is crucial for disasters such as the Deepwater Horizon, where manual inspection of the disaster site would be completely impossible.

With robots just beginning to replace humans in dangerous and high-risk environments, the potential for future improvement is clearly visible. Using teleoperated robots keeps the human operators out of harms way and gives them access to task-specific sensors and equipment that would otherwise be unavailable. Without worrying about his or her personal safety, the operator is able to devote his or her full attention to the mission and focus on making the rescue effort continue as smoothly as possible. In the future, a human operator may not be needed at all: full autonomy will automate the monotonous

drudgery of disaster recovery and let humans focus on the tasks that are most important.

7 Acknowledgments

This project would not have been possible without the support of Dr. Predrag Spasojevic as our faculty adviser or the help of the members of Rutgers IEEE Student Branch. I am particularly grateful for Adam Stambler's excellent leadership, Peter Vasilnak's mechanical design, and the faculty support of Dr. Kristin Dana, Joe Lippencott, Steve Orbine, John Scafidi, and Dr. Stuart Shalat. I would also like to thank our sponsors for their generous contributions: Rutgers Engineering Governing Council, Knotts Corporation, 80/20 Inc., Optima Batteries, Github, IEEE Region 1, Novatel, and Omnistar.

References

- [1] OV7720 VGA Product Brief. 4 2008.
- [2] Eriko Guizzo. Japan Earthquake: Robots Help Search For Survivors. *IEEE Spectrum*, 3 2011.
- [3] Eriko Guizzo. Japanese Robot Surveys Damaged Gymnasium Too Dangerous for Rescue Workers. *IEEE Spectrum*, 5 2011.
- [4] Richard Hart. Robot could assist in quake search and rescue. *MSNBC*, 1 2010.
- [5] Ray C. He. *Stereo vision and mapping with unsynchronized cameras*. PhD thesis, Massachusetts Institute of Technology, 2008.
- [6] Albert Huang. *Lane Estimation for Autonomous Vehicles Using Vision and LIDAR*. PhD thesis, Massachusetts Institute of Technology, 2010.
- [7] A.S. Huang, D. Moore, M. Antone, E. Olson, and S. Teller. Multi-sensor lane finding in urban road networks. *Proceedings of Robotics: Science and Systems*, Zurich, Switzerland, 2008.
- [8] K. Konolige. Small Vision Systems: hardware and implementation. *Eighth International Symposium on Robotics Research*, 10 1997.
- [9] John Roach. A robot cut out for mine rescue work. *MSNBC*, 11 2010.
- [10] R.B. Rusu, Z.C. Marton, N. Blodow, M. Dolha, and M. Beetz. Towards 3D Point cloud based object maps for household environments. *Robotics and Autonomous Systems*, 56(11):927–941, 2008.
- [11] David Schneider. Robin Murphy: Roboticist to the Rescue. *IEEE Spectrum*, 2 2009.
- [12] Bernard Theisen. The 19th Annual Intelligent Ground Vehicle Competition, 2011.